Small Structures

small structures

www.small-structures.com

RESEARCH ARTICLE OPEN ACCESS

Nonlinearity Matters in Light–Matter Interaction: Multiphoton 3D Lithography

Michalis Stavrou[1,2] | Efrosyni Pramatioti[3,4] | Gordon Zyla[2] | Dimitra Ladika[2] | Georgios Skentzos[3,4] | Maria Farsari[1] | Saulius Juodkazis[2,5,6] | Mangirdas Malinauskas[2] | David Gray[1] | Stelios Couris[3,4]

[1]Foundation for Research and Technology-Hellas (FORTH), Institute of Electronic Structure and Laser, Heraklion, Greece | [2]Laser Nanophotonics Group, Laser Research Center, Physics Faculty, Vilnius University, Vilnius, Lithuania | [3]Non-Linear Optics and Laser Applications Laboratory (NLOLA), Department of Physics, University of Patras, Greece | [4]Institute of Chemical Engineering Sciences (ICE-HT), Patras, Greece | [5]Melbourne Center for Nanofabrication (MCN), Clayton, Australia | [6]Optical Sciences Centre, Swinburne University of Technology, Hawthorn, Australia

Correspondence: Michalis Stavrou (m.stavrou@iesl.forth.gr) | Mangirdas Malinauskas (mangirdas.malinauskas@ff.vu.lt) | David Gray (dgray@iesl.forth.gr) | Stelios Couris (couris@upatras.gr)

Received: 21 January 2026 | **Revised:** 9 March 2026 | **Accepted:** 30 March 2026

Keywords: 3D printing | charge transfer complex | direct write lithography | energy deposition | nonlinear parameters | rayleigh length | super-resolution

ABSTRACT

Multiphoton 3D lithography (MP3DL) based on ultrafast nonlinear light-matter interactions to enable micro-/nano-structuring with resolution beyond the diffraction limit, yet the physical origin of the nonlinear energy deposition that initiates polymerization in photoresists remains ambiguous. Here, we investigate the optical nonlinearities governing MP3 DL using SZ2080^{TM}, a widely used hybrid organic–inorganic photoresist in micro-/nano-fabrication. Both the pure resist and formulations containing the photoinitiators/photosensitizers Irgacure369 and 4,4′-bis(diethylamino)benzophenone are characterized by Z-scan technique. The nonlinear absorption and refraction coefficients are experimentally determined at commonly used femtosecond laser wavelengths (515, 800, and 1030 nm) under different focusing configurations. These coefficients reveal energy deposition particularities, indicating that the majority of deposited energy originated from the resist itself and can be further enhanced through strong interaction with the photoinitiator, particularly via charge transfer effects. Additionally, we show that nonlinear energy deposition can be substantially increased by extending the interaction volume through an increased beam Rayleigh length, providing an alternative route for improving MP3DL efficiency. Our findings challenge the conventional assumption that photo-polymerization is initiated exclusively by photoinitiators and establish the fundamental basis for photo-initiator-free 3D laser lithography, offering predictive guidelines of polymerization conditions and accelerating the design and optimization of advanced micro-/nano-fabrication.

1 | Introduction

The breakthrough advancement in additive manufacturing (AM) has ignited a revolution across various scientific disciplines and industrial sectors [1–4]. Among AM approaches, multiphoton polymerization 3D lithography (MP3DL) distinguished by its rapid prototyping, free-form fabrication of intricate 3D structures with feature size below 100 nm and spatial resolution beyond the diffraction limit, minimal material waste, and cost-effective low-volume production [5–8]. These features have made MP3DL indispensable in applications requiring microscale and nanoscale precision, such as biomedical scaffolds [9], microoptics [10, 11], metamaterials [12, 13], electromechanical systems [14], and microfluidics [15].

MP3DL leverages the effectiveness of the nonlinear mechanism of multiphoton absorption (MPA) to enable otherwise forbidden electronic transitions in a photosensitive resin/resist, achieved using femtosecond (fs) laser radiation at wavelengths that correspond to the material's transparency window. In this nonlinear regime, the material's response deviates from the linear Beer–Lambert law, and the absorption coefficient α [cm^{-1}] becomes

intensity-dependent, described as: $\alpha = \alpha_0 + \beta I + \gamma I^2 \ldots$, where α_0 [cm^{-1}] is the linear absorption coefficient, and β [cm/W], γ [cm^3/W^2], and so on, correspond to two-photon absorption (2 PA), three-photon absorption (3 PA), and higher-order nonlinear coefficients, respectively [16, 17]. These nonlinearities cause opacity at wavelength where the material is normally transparent ($\alpha_0 \approx 0$), thus increasing energy deposition within the focal volume and initiating in situ polymerization [18–20].

To facilitate this process, photosensitizers/photoinitiators are added at low concentrations, typically ranging from 0.1 to 2% w/w in respect to the polymer. These additives decrease the absorption depth and the order of MPA, as well as contribute to nonlinear ionization scenarios, such as multiphoton ionization, tunneling, inverse Bremsstrahlung, impact ionization, and avalanche ionization [21]. These processes collectively enhance the energy deposited within the prepolymer matrix, leading effectively to generation of free radicals, either directly or via ionization channels [22].

The deposited energy dose per pulse is defined by the n-photon absorption coefficients $\alpha^{(n)}$ and cross sections $\sigma^{(n)}$, which are directly related to the absorption rate and the probability of n-photon transition. These MPA coefficients substantially influence the polymerization rate (R), which defines the effective voxel size and scales with the light intensity raised to the power of the absorption order $R \propto \sigma^{(n)} I^n$ [23]. In parallel, the voxel dimensions are further influenced by high-intensity induced nonlinear refraction effects, which change the refractive index n of the material according to $n = n_0 + n_2 I$, where n_0 is the linear refractive index and n_2 is the nonlinear refractive index [16, 17]. This refractive response arises from instantaneous interactions with bound electrons (Kerr effect) or from free-carrier generation, both of which can change the beam propagation and the spatial definition of the focal volume. Consequently, the nonlinear absorption and refraction properties undoubtedly affect the threshold of polymerization, the range of usable processing parameters (e.g., scan velocity and fabrication window), and ultimately the spatial resolution achievable in 3D microstructure fabrication. These properties offer an experimental basis for explaining the multiphoton lithography (MPL) behavior of non-photosensitized and photosensitized resists under excitation by amplified-pulse lasers [24] and high-repetition-rate ultrafast laser oscillators [25].

The knowledge of multiphoton properties is also essential for determining the precise conditions for the most effective energy deposition—accounting for cumulative contributions from both the photosensitizer and host polymer, as recently verified—thus facilitating fine-tuned control over the fabrication process [26]. These properties exhibit wavelength dependencies due to quantum mechanical selection rules that dictate the transition dipole moments between molecular states of different symmetries [27]. Additionally, they depend on pulse duration, which influences the timescale of the instantaneous electronic cloud distortion, and on repetition rate, where high repetition frequencies (on the order of MHz) lead to thermal buildup [28, 29]. Additionally, the effective interaction volume within the sample, defined by the beam waist and Rayleigh range, could significantly affect the cumulation of nonlinear absorption and refraction, and consequently the threshold intensity of multiphoton polymerization.

Therefore, the accurate characterization of nonlinear optical parameters in commonly used resists and photosensitized materials—often overlooked in the broader manufacturing community due to the lack of standardized methods—emerges as a holistic approach for selecting optimal fabrication conditions. This includes the tuning of key parameters such as peak intensity, excitation wavelength, pulse duration, and the numerical aperture (*NA*) of the objective lens, all of which are essential for achieving high resolution and energy-efficient multiphoton lithography. In combination with the growing concerns raised for human health and environmental impacts associated with photosensitizers—particularly toxic aromatic polycyclic hydrocarbons commonly used in 3D printing [30]—a deeper understanding of energy deposition in photoresist, achieved through the characterization of their nonlinear optical properties, could support the development of a more sustainable, initiator-free AM approach exploiting fs-lithography.

In this context, we present a comprehensive investigation of the optical nonlinearities governing multiphoton 3D lithography using SZ2080™ photoresist, a widely used hybrid organic–inorganic photoresist in 3D micro-/nano-fabrication. We examine both the pure resist, and its formulations containing the photoinitiators IRG369 and BIS (Irgacure369 and 4,4′-bis(diethylamino)benzophenone or Michler's ketone). By employing Z-scan technique, we determine, for the first time, the nonlinear absorption and refraction coefficients at all commonly used laser wavelengths (i.e., 515, 800, and 1030 nm) of fs laser sources. We also assess, for first time, the role of focusing conditions (i.e., the beam Rayleigh range) on the effective interaction volume (by performing MPL and Z-scan experiments with different focusing conditions), which dictates the spatial confinement of energy deposition and the onset of nonlinear response.

Our findings provide experimental evidence that pure SZ2080™ photoresist can initiate polymerization under broadband irradiation through two-, three- and four-photon absorption processes without the use of photoinitiators, providing insight into the physics behind previously reported initiator-free laser-based polymerization [24, 25]. Additionally, we further show that extending the Rayleigh range facilitates more energy-efficient fabrication by decreasing peak intensities while maintaining sufficient nonlinear excitation. This approach reduces energy consumption and mitigates photodamage, enhancing throughput. Most importantly, the determined β and n_2 for pure resist and its mixtures offer a foundation for exact energy deposition modeling and process optimization in nonlinear laser-based lithography as they define both the spatial and temporal evolution of laser intensity within the resist. Understanding how the nonlinear optical properties vary with the interaction volume allows for their correlation with any possible focusing condition used in MP3DL, thus enabling accurate control of fabrication process. These nonlinear coefficients for pure and photosensitized resists also provide a deeper understanding of the mechanisms of polymerization process, contributing to the interpretation of prior reports in laser-based polymerization [19, 20, 31–33].

2 | Experimental Section

2.1 | Multiphoton Absorption and Nonlinear Refraction Measurements

2.1.1 | Z-Scan Methodology and Theoretical Formulation

The Z-scan technique is widely used for assessing the intensity-dependent variations in sample's absorbance α and refractive

index n induced by nonlinear effects under irradiation with an intense laser beam [34].

A simplified schematic of a typical Z-scan setup is presented in Figure 1A. In this configuration, the sample is translated along the propagation direction of a focused laser beam (z-axis) using a computer-controlled translation stage so that it is exposed to different on-axis intensities at each position relative to the focal plane ($z = 0$). As the sample moves towards the focus, the increasing radiation intensity causes changes in its transmittance. The outgoing from the sample laser beam is then divided by a 50:50 non-polarizing beam splitter, allowing these transmittance variations to be measured simultaneously by two distinct experimental configurations: the 'Open-Aperture' (OA) and 'Closed-Aperture' (CA) Z-scans. In the OA Z-scan arm, the full transmitted radiation is collected by a lens and monitored by a photodiode, providing a measurement of the sample's n-photon absorption coefficients (e.g., $\beta : 2PA$, $\gamma : 3PA$, $\delta : 4PA$). Simultaneously, in the CA Z-scan arm, a small diameter pinhole (1 mm, in our case) placed in the far field allows only the central portion of the beam to reach the detector, making the measurement sensitive to phase-front distortions and thus enabling the determination of the sample's nonlinear refractive index n_2.

For a Gaussian-shaped temporal pulse, the normalized OA Z-scan transmittance expressions for processes of 2, 3, and 4 PA are given in Equations (1), (2) and (4), respectively [35, 36]

$$T(z) = \frac{1}{\sqrt{\pi}\left(\frac{\beta I_0 L_{\text{eff}}}{1+(z/z_R)^2}\right)} \int_{-\infty}^{+\infty} \ln\left(1 + \frac{\beta I_0 L_{\text{eff}}}{1+(z/z_R)^2} e^{-t}\right) dt \quad (1)$$

$$T(z) = \frac{1}{\sqrt{\pi}\sqrt{2\gamma L\left(I_0 \frac{w_0^2}{w^2(z)}\right)^2}} \int_0^1 \frac{R\left(\frac{z}{z_R}\right)}{\left(\frac{z}{z_R}\right)\sqrt{-\ln\left(\frac{z}{z_R}\right)}} d\left(\frac{z}{z_R}\right) \quad (2)$$

where,

$$R\left(\frac{z}{z_R}\right) = \ln\left[\sqrt{1 + 2\gamma L (I_0 w_0^2/w^2(z))^2 \left(\frac{z}{z_R}\right)^2} + \sqrt{2\gamma L (I_0 w_0^2/w^2(z))^2 \left(\frac{z}{z_R}\right)^2}\right] \quad (3)$$

$$T(z) = \frac{1}{3\sqrt{\pi}\sqrt[3]{3\delta L (I_0 w_0^2/w^2(z))^3}} \int_0^1 \frac{R(\Delta)}{z/z_R\sqrt{-\ln(z/z_R)}} dz \quad (4)$$

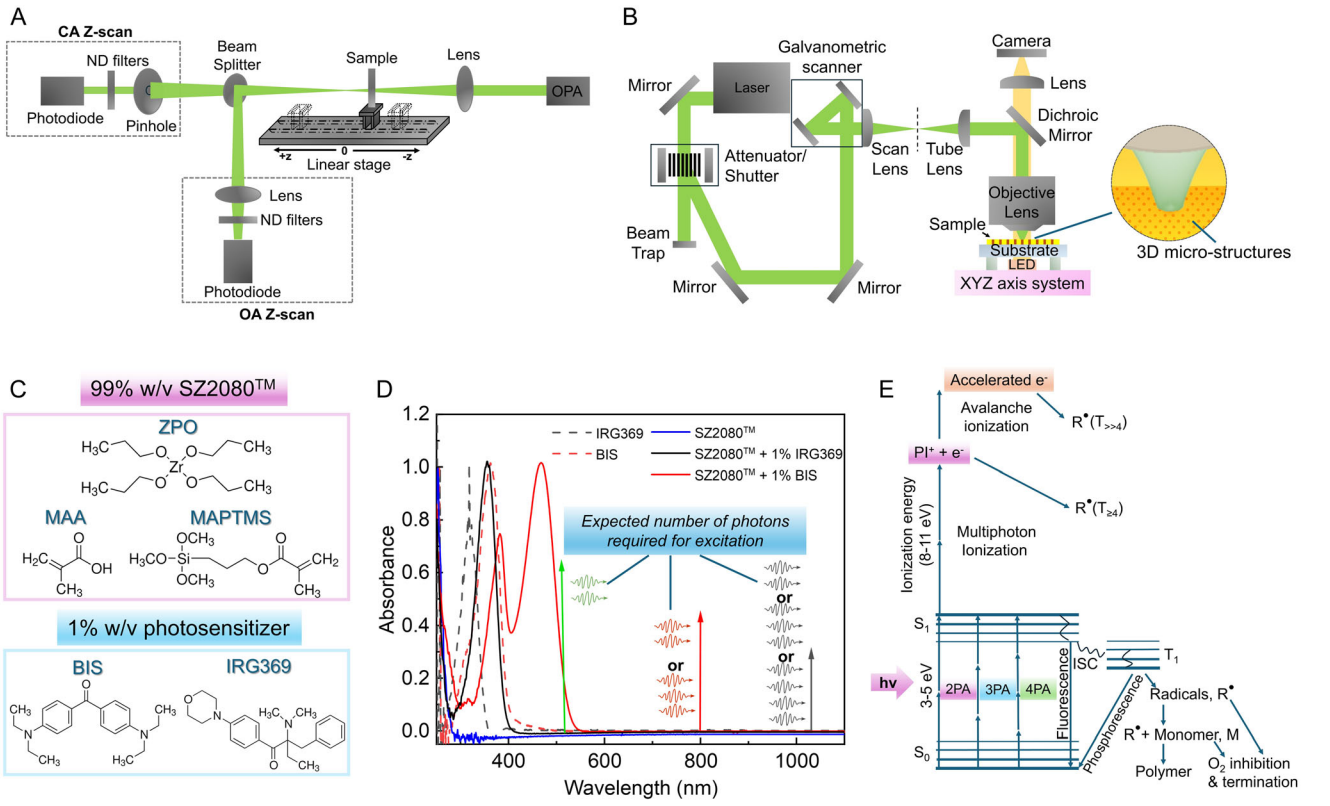

FIGURE 1 | (A) Schematic representation of the Z-scan setup simultaneously measuring intensity-dependent transmittance variations due to nonlinear absorption (OA Z-scan) and refraction (CA Z-scan). (B) Experimental configuration of the MPL setup used for precise layer-by-layer 3D micro/nanofabrication. (C) Molecular structures of the SZ2080^{TM} resist components (ZPO, MAA, and MAPTMS) and the photosensitizers BIS and IRG369. (D) UV–VIS-NIR absorption spectra (250–1100 nm) of IRG369 and BIS solutions in DCM, along with the corresponding spectra for films of neat SZ2080^{TM} prepolymer and SZ2080^{TM} mixed with 1 wt% IRG369 and BIS photosensitizers. The solution samples had a thickness of 1 mm and the films a thickness of ≈14 μm. The arrows indicate the excitation wavelengths and the corresponding number of photons required for excitation at each wavelength. (E) Photo-physical pathways resulting in the generation of free radicals, including n-photon absorption and intersystem crossing, as well as multiphoton or avalanche ionization under very high-intensity laser irradiation.

where,

$$R(\Delta) = \ln\left(\frac{\sqrt{\Delta^2(z/z_R)+\Delta(z/z_R)+1}}{\Delta(z/z_R)-1}\right) - \sqrt{3}\arctan\left[\frac{2\Delta(z/z_R)+1}{\sqrt{3}}\right] + \frac{\sqrt{3}\pi}{2} \quad (5)$$

$$\Delta(z/z_R) = (1+(3\delta L(I_0 w_0^2/w^2(z))^3)(z/z_R)^3)^{-1/3} \quad (6)$$

The transmittance recorded in the CA Z-scan is theoretically described by Equation (7) [36]

$$T(z) = 1 - \frac{4n_2 k I_0 L_{eff}\frac{z}{z_R}}{\left[1+\left(\frac{z}{z_R}\right)^2\right]\times\left[9+\left(\frac{z}{z_R}\right)^2\right]} \quad (7)$$

In these equations, L_{eff} is the sample's effective length, I_0 is the on-axis peak irradiance, z_R is the Rayleigh length, w_0 is the beam radius at the focus, and $k = 2\pi/\lambda$ is the excitation wavenumber. The dimensions of the parameters used in SI units are given here: z_0,L_{eff} [m], k [m^{-1}] n_0 [none], I_0 [W/m^2], β [m/W], γ [m^3/W^2], δ [m^5/W^3], n_2 [m^2/W].

From the n-photon absorption coefficients α_n, determined by fitting the OA Z-scan recordings with Equations (1), (2) and (4), the corresponding n-photon absorption cross-section σ_n is calculated through Equation (8) [35]

$$\sigma_n = \frac{\alpha_n(h\nu)^{n-1}}{N_A\rho} \quad (8)$$

where h [in J·s] is the Plank's constant, ν [in s^{-1}] is the frequency of light, N_A [in mol^{-1}] is the Avogadro number and ρ [in M] is the molar concentration. The σ_2 is measured in the Goeppert Mayer (GM) units (1 GM = 10^{-50} cm^4·s·$photon^{-1}$).

2.1.2 | Laser Source

Z-scan measurements were conducted at wavelength relevant to commercial laser-based 3D printing systems: ~1030, 800, and 515 nm. Specifically, for excitation at 800 nm, the fundamental output of a chirped-pulse amplification Ti:sapphire laser system (Trident X, Amplitude Technologies) was used directly, while the other wavelengths generated through an optical parametric amplifier (OPA, Palitra, Amplitude Technologies), pumped by the same Ti:sapphire laser source. Pulse durations at each wavelength were measured just prior to the sample using an autocorrelator and found to be approximately 80 fs. The pulse repetition rate was as low as 10 Hz. Thus, only ultrafast (instantaneous) material responses arising from the electronic interactions with the laser radiation can be measured, effectively excluding thermal induced effects.

To elucidate how the axial extent of nonlinear energy deposition—depends on the beam's Rayleigh range—impacts the multiphoton polymerization efficiency, Z-scan experiments were performed using two different focusing configurations. A 20 cm focal-length apochromatic lens yielded beam waists of ~40, 20, and 30 μm at 515, 800, and 1030 nm, respectively, corresponding to Rayleigh ranges of ~9.8, 1.6, and 2.7 mm. In contrast, tighter focusing with a 2.5 cm lens resulted in beam waists of ~13, 6.5, and 9 μm at the same wavelengths, decreasing the Rayleigh ranges to ~1.0, 0.17, and 0.25 mm, respectively. From the measured pulse duration and focal spot size at each wavelength, the corresponding peak intensities using the 20 cm focal length lens were estimated to range from 0.65 to 1.9 TW/cm^2 at 515 nm, 0.9–1.7 TW/cm^2 at 800 nm, and 1.8–3.0 TW/cm^2 at 1030 nm. When the 2.5 cm focal length lens was employed, approximately twice the peak intensities were required to achieve comparable transmittance modulations.

2.2 | MPL Fabrication Process

2.2.1 | MPL Experimental Setup for 3D Microstructuring

As shown in Figure 1B, which depicts a schematic of the MPL setup, the 3D manufacturing process involves irradiating a photosensitive resist with a tightly focused femtosecond laser beam, triggering nonlinear absorption exclusively at the focal point. Consequently, the increased deposition of energy to the intended voxel induces spatially confined polymerization and prevents photo-curing in the surrounding region. High speed patterning within each layer is achieved using a 2D galvanometric scanner (Hurryscan II 10, Scanlab, Germany), which precisely deflects the focused laser beam at high speeds. 3D stacking is performed by employing a high-precision piezoelectric stage (M-605.1DD, Physik Instrumente, Germany), which allows for the precise vertical (z-axis) translation between successive layers.

To preserve beam collimation and ensure a uniform scanning field, an f-theta lens (Sill Optics) and a tube lens (Thorlabs) were combined and positioned into the beam's propagation path. An acoustooptical modulator (AOM, AA Opto Electronics, France) offered high-speed shuttering and dynamic power modulation to controlling regulate exposure. All entire 3D printing workflow, including power modulation, scanning, and stage translation, was coordinated using a commercial software (*Arachne*, Biomimetics, Greece), enabling highly reproducible printing of microstructures.

To assess polymerization threshold and voxel-size of the different photosensitized resists, bridge structures were printed using a single-scan exposure writing strategy, consisting of a continuous scan trajectory without volumetric slicing or hatching. The polymerization threshold was evaluated from single-pass polymerization lines written under identical focusing (NAs of 0.45 and 1.4) and scanning speed (5000 μm/s) conditions while systematically varying the laser power from the minimum exposure condition resulting in a continuous and mechanically stable suspended bridge until the power that induces visible photodamage.

3D demonstrations with or without photoinitiator involved the fabrication of woodpile photonic crystals and complex scaffolds. Woodpile photonic crystals were printed using a layer-by-layer single-line writing approach, in which each rod was defined by an individual scan trajectory following a predefined pattern (i.e., stacked arrays of parallel rods, where each subsequent layer is rotated by 90° relative to the preceding layer and laterally displaced by half a lattice period). In contrast, the complex 3D scaffolds were produced using a conventional volumetric fabrication strategy with slicing and hatching, using a hatch spacing and slice spacing of 0.1 μm. For these experiments, the scanning speed was kept constant at 5000 μm/s. The laser beam was focused into the samples using an objective of NA = 1.4. High fidelity 3D structures were systematically achieved using a range of peak intensities between 1.5–2 TW/cm^2.

2.2.2 | Laser Source for 3D Printing

The excitation wavelengths selected for the 3D printing demonstrations were identical with those used for the nonlinear optical studies, allowing directly correlation of multiphoton properties and polymerization initiation performance. Two different fiber laser systems were used for 3D patterning via MPL. The first was an Er:Yb co-doped fiber laser (FemtoFiber ultra 780, Toptica Photonics AG) operating at 800 nm (frequency doubling of the fundamental output at 1560 nm), with a pulse width of 150 fs and a repetition rate of 80 MHz. The second was a Yb-doped fiber laser (Pharos, Light Conversion) emitting 300 fs laser pulses at 1030 nm with a repetition rate of 200 kHz. This system was integrated with a second-harmonic generation module to enable operation at 515 nm. Note that under high-repetition rate excitation, particularly in the MHz regime, cumulative thermal effects may enhance energy deposition that initiate polymerization. Consequently, the observed polymerization threshold and voxel morphology is a convolution of multiphoton absorption and secondary time-dependent dynamics. Under these conditions, MPL demonstrations are intended as qualitative validation of wavelength-dependent nonlinear energy deposition trends, rather than a strict one-to-one comparison of intrinsic material sensitivity across wavelengths.

To demonstrate how the axial confinement of energy influence the MPL performance, specifically the power threshold of polymerization, two microscope objective lens with different NAs were employed: a high-NA lens (63×, $NA = 1.4$) and a low-NA lens (20×, $NA = 0.45$). The latter resulted in Rayleigh lengths of 3.1 μm at 515 nm, 4.8 μm at 800 nm, and 6.2 μm at 1030 nm, while tighter focusing reduced these values by 10 times, as in the Z-scan experiments. This enables a direct quantification of how the variations in nonlinear coefficients with the effective interaction volume influence the polymerization threshold.

2.3 | Materials and Samples Preparation

2.3.1 | Synthesis of SZ2080^{TM}-Based Resists

The benchmark hybrid organic–inorganic SZ2080^{TM} photoresist was selected to explore the physical processes underlying laser-based polymerization [37]. As presented in Figure 1C, this hybrid composite formulated from zirconiumn-propoxide (ZPO, 70% in propanol), which is the organic precursor, and methacryloxypropyl trimethoxysilane (MAPTMS, 97%) together with methacrylic acid (MAA, 99%), which form the inorganic component. The molar ratios of the components used to synthesize this hybrid network were MAPTMS:ZPO = 8:2 and ZPO:MAA = 1:1. Firstly, MAPTMS was hydrolyzed by adding HCl (0.1 M), followed by stirring for 15 min. In a different flask, ZPO was chelated with MAA in the presence of 1-propanol (145 μL) and stirred for 20 min. The hydrolyzed MAPTMS was subsequently added dropwise to the ZPO solution, and the mixture was stirred for a further 20 min. The resulting composite was finally filtered using 0.22 μm pore-size membranes.

The compounds 4,4′-bis(diethylamino)benzophenone (BIS) and Irgacure 369 (IRG369), whose molecular structures are presented in Figure 1C, were used as photosensitizers at a concentration of 1% w/w to the solution of hybrid composite.

2.3.2 | Sample Preparation for Z-Scan and MPL

Two kind of samples were prepared for the Z-scan measurements: (*i*) thin films of pure SZ2080^{TM} and mixtures containing 1 wt% IRG369 or BIS, deposited on 0.14 mm glass substrates by spin coating at 5000 rpm for 45 s, and (*ii*) 3 mM solutions of BIS and IRG369 in dichloromethane (DCM), placed in 1 mm path-length quartz cells. The thickness of the films were measured by a profilometer (Mitutoyo SJ-410), yielding a value of ≈14 μm.

For MPL, the samples were prepared by drop-casting the pure and photosensitized SZ2080^{TM} prepolymers onto silanized 0.14 mm glass substrates. The samples were left to rest under low-vacuum conditions until their gelation as the solvent evaporated. After fabrication, the droplets were developed in 4-methyl-2-pentanone for 30 min to remove the unpolymerized resist.

3 | Results and Discussion

3.1 | UV–VIS-NIR Absorption Spectra

First, the interaction of the photosensitizers with the prepolymer matrix was examined by characterizing their linear absorption properties. For this purpose, the UV–VIS-NIR absorption spectra of neat BIS, IRG369, and SZ2080^{TM} as well as their mixtures were measured, as show in Figure 1D. The photosensitizers, each dissolved at a concentration of 3 mM in DCM, exhibit broad absorption bands lying in the UV region, with maxima at 362 nm (BIS) and 318 nm (IRG369), arising from $\pi \rightarrow \pi^*$ transitions of their aromatic chromophores [38]. The red-shifted spectrum of BIS indicates its greater aromaticity and more extended π-electron delocalization relative to IRG369.

Similarly, the corresponding spectra of thin films composed of neat and photosensitized SZ2080^{TM} show intense absorption features in the UV. These attributed to $\pi \rightarrow \pi^*$ transitions of the aromatic C = C bonds in the methacrylate groups, $n \rightarrow \pi^*$ transitions from non-bonding electrons on the carbonyl oxygen (C = O) groups in MAPTMS and MAA, as well as $n \rightarrow \sigma^*$ transitions from oxygen lone-pair orbitals into the σ^* anti-bonding orbital of the Zr–O bond in ZPO. Interestingly, the results demonstrated that mixing SZ2080^{TM} with 1 wt% BIS yielded a new absorption band which was absent in either component alone. This band is most probably attributed to charge transport between strong electron-donating dimethylamino groups of BIS and the electron-deficient ZPO component of SZ2080^{TM}. As the new absorption band is located in the visible region, it provides strong evidence for the formation of a charge transfer state arising from donor–acceptor interactions [39]. Other processes, such as solvatochromism, can be excluded, as they typically shift existing bands rather than generate entirely new absorption features [40]. Similar donor–acceptor complex formation has been also reported in other π-conjugated complex systems mixed with fullerene molecules [41]. It is noteworthy that the addition of 1 wt% IRG369 to the SZ2080^{TM} solution did not form any new absorption features, consistent with the weaker electron-donating strength of IRG369 compared to BIS.

Furthermore, it was observed that the peaks of BIS and IRG369, which were initially located at 362 and 318 nm, present red-shifts of about 20 and 36 nm, respectively, after mixing with the prepolymer material (i.e. the chemical precursor). These shifts likely result from a combination of factors, including the known

sensitivity of Michler's ketone and Irgacure derivatives to changes in the local dielectric environment [38, 42], van der Waals interactions between the aromatic rings of the photosensitizers and the methacrylate groups of the prepolymer, as well as hydrogen bonding between the amine groups of the photosensitizers and silanol groups resulting from the hydrolysis of MAPTMS.

Above 515 nm, where is located the stimulated emission spectral region of Ti:Sapphire crystals and Yb/Er:Yb-doped fibers, the single-photon absorption of SZ2080^{TM} and its photosensitized formulations is negligible. Therefore, the electronic transitions at these wavelengths proceeds predominantly through n-photon (nonlinear) absorption, as shown in Figure 1E, where the transition probability from the ground singlet state (S_0) to the first excited singlet state (S_1) scales proportionally to the corresponding n-photon absorption cross-sections and the photons energy. From S_1, the molecule undergoes transition to the first excited triplet state (T_1) via intersystem crossing (ISC), from which homolytic bond cleavage occurs, producing free radicals that trigger polymerization. At sufficiently high laser intensities, polymerization may also be initiated through photoionization-driven pathways. However, in this case, the lateral voxel dimension is expanded due to free-carrier-induced nonlinear refractive index variations, which reduces the printing resolution [32].

By inspecting the absorption spectra, valuable insights into the order of multiphoton absorption for the different excitation wavelengths can be obtained

- At 515 nm, the lowest-energy required for optical transitions in both pure and photosensitized SZ2080^{TM} can be mainly reached through 2 PA, given that the single-photon absorption is minimal at this wavelength and the accessible excited states lie at energy corresponding to half of the excitation wavelength ($0.5\lambda = 258$ nm).
- At 800 nm, three photons are required for initiating electronic transitions in pure SZ2080^{TM} and SZ2080^{TM} containing 1 wt% IRG369, as resonance absorption occurs only when the condition $0.33\lambda = 267$ nm is satisfied. In contrast, the addition of 1 wt% BIS into the SZ2080^{TM} prepolymer reduces the order of MPA, allowing for electronic transitions to proceed effectively via 2 PA.
- At 1030 nm, pure SZ2080^{TM} requires 4 PA to reach the lowest allowed excited states ($0.25\lambda = 257$ nm). In contrast, the presence of photosensitizers reduces the multiphoton order: in SZ2080^{TM}-BIS, the formation of the charge transfer band in the visible enables excitation via 2 PA (2PA; $0.5\lambda = 515$ nm), while in SZ2080^{TM}-IRG369, the presence of resonant states at the 1/3 of the excitation wavelength ($0.33\lambda = 343$ nm) supports optical transitions via 3 PA.

3.2 | Multiphoton Absorption Properties

Figure 2A–F shows representative OA Z-scan curves for thin films of pure SZ2080^{TM} and SZ2080^{TM} mixed with 1 wt% BIS and IRG369. These Z-scans were taken using ~80 fs laser pulses at three excitation wavelengths relevant to MPL (i.e., 515, 800, and 1030 nm) under two different focusing configurations, where the Rayleigh ranges differed by approximately an order of magnitude. For the sake of simplicity, only recordings obtained at incident peak intensities below the nonlinear absorption thresholds of the glass substrate at each wavelength, or those exhibiting only weak glass absorption signals, are presented here. As shown, the transmittance decreases as the samples approach the focal plane, where the laser intensity becomes progressively higher, deviating from the Beer–Lambert regime (represented by the plateau far from the focus) and reaching its minimum at the focal point ($z = 0$). This behavior denotes reverse saturable absorption (RSA), typically assigned to MPA and/or excited state absorption. However, since the latter process involves energy absorption from an already excited state, its contribution to RSA can be rather ruled out since fs laser pulses do not allow for significant accumulation of intermediate excited-state population [16]. Therefore, n-photon absorption is the main contributor to the reduced samples' transmittance, with the specific n-photon process involved being determined by the incident laser wavelength, as previously discussed.

To experimentally determine the n-photon absorption order predicted by the absorption spectra for each excitation wavelength, the OA Z-scan recordings were fitted with the corresponding two-, three-, and four-photon absorption models given in Equations (1), (2) and (4) . From these fits, it is evident that the OA Z-scan traces of SZ2080^{TM} are best described by the theoretical models of 2 PA at 515 nm, 3 PA at 800 nm, and 4 PA at 1030 nm. In the presence of 1 wt% IRG369, the n-photon absorption order in the infrared is decreased, with the fits showing 2 PA at 515 nm and 3 PA at both 800 and 1030 nm. The most pronounced decreased is observed for the SZ2080^{TM}-BIS mixture, where 2 PA dominates at all three irradiation wavelengths.

To further quantify and distinguish the contributions of the prepolymer matrix and photosensitizers to energy deposition, OA Z-scans of IRG369 and BIS solutions were separately measured under similar excitation conditions. The corresponding recordings, presented in Figure S1, reveal that BIS exhibits 2 PA at both 515 and 800 nm and 3 PA at 1030 nm, while IRG369 exhibits 2 PA at 515 nm and 3 PA at 800 and 1030 nm.

By fittings all OA Z-scan data obtained at different laser peak intensities, the n-photon absorption coefficients of pure and photosensitized SZ2080^{TM} were determined, and the results are presented in Figure 2G–I. To facilitate a straightforward comparison, mean values were also obtained by averaging the nonlinear coefficients over all laser intensities, and these averages are gathered in Table 1 along with the corresponding coefficients of the neat photosensitizer. The corresponding n-photon absorption cross sections were then calculated from these coefficients and are also listed in the same Table. From these values, possible contributions from the glass substrate and DCM to the nonlinear absorption have been removed.

As shown, pure SZ2080^{TM} prepolymer exhibits intrinsic nonlinear absorption—2 PA at 515 nm, 3 PA at 800 nm, and 4 PA at 1030 nm—indicating its capability to initiate polymerization even in the absence of an added photosensitizer. Adding 1% wt of BIS and IRG369 to the prepolymer led to a substantial increase in the nonlinear absorption coefficients under both focusing regimes. Under visible irradiation, the values of β and σ were found to present an enhancement by approximately an order of magnitude. In contrast, under near-infrared irradiation, the effective order of multiphoton absorption decreased due to interactions between the prepolymer and the photosensitizers, which implies stronger nonlinear absorption contributions relative to the higher-order processes in pure SZ2080^{TM}. Notably, the n-photon absorption cross sections of the photosensitized resists, which represent a

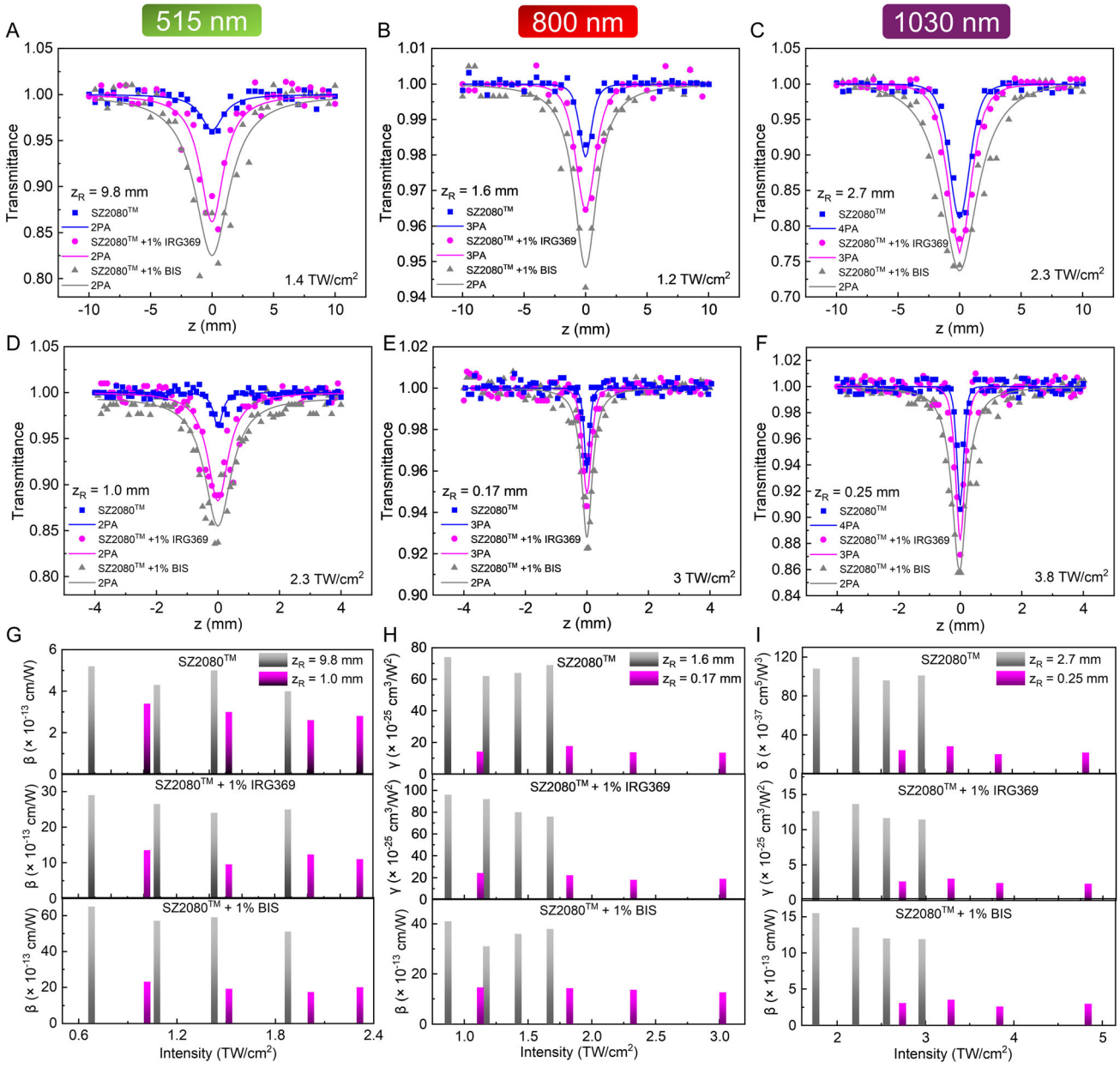

FIGURE 2 | OA Z-scan recordings and n-photon absorption coefficients of SZ2080™ with and without photosensitizers under different laser peak intensities and two focusing configurations at (A), (D), (G) 515 nm, (B), (E), (H) 800 nm, and (C), (F), (I) 1030 nm. Tighter focusing required significantly higher intensities to detect nonlinear absorption signal.

figure of merit as they are independent of the molecular concentration, were found to be comparable to or significantly enhanced than those of the individual photosensitizers under all excitation wavelengths. This clearly indicates that the deposited energy in 3D printing has cumulative contributions from both the photosensitizer (with weight fraction $f \approx 1\%$) and from the prepolymer matrix (with fraction $1 - f \approx 99\%$). However, owing to its significantly larger weight fraction, the prepolymer dominates the nonlinear optical response (see evaluation of quantitative contributions in Supplementary Information). Thus, it is demonstrated beyond doubt that polymerization can be effectively initiated across a broad spectral window without the need of potentially toxic photosensitizers.

Among the photosensitized resists, the SZ2080™-BIS mixture exhibited nearly double the two-photon coefficients in the visible. In the near-infrared region, it further showed a lower nonlinear absorption order (i.e., 2 PA) than that of the SZ2080™-IRG369 formulation, indicating that a lower dose of energy per pulse is required for triggering nonlinear effects. This enhanced performance is likely attributed to the formation of a donor–acceptor complex as previously discussed. Particularly, the two electron-rich dimethylamino substituents of BIS strongly interact with the electron-deficient ZPO component of SZ2080™, leading to the formation of an intermolecular donor–acceptor complex. These interactions may stabilize a charge transfer state that appear at longer wavelengths relative to the absorption bands of the individual donor and acceptor molecules (see absorption spectrum of SZ2080™-BIS resist). Due to the formation of these low-energy electronic states, the BIS-containing sample can undergo more efficient electronic transitions via 2 PA pathways under near-infrared

TABLE 1 | Nonlinear optical parameters of the neat SZ2080^{TM} pre-polymer, SZ2080^{TM} mixed with the photosensitizers BIS and IRG369, and the individual photosensitizers, obtained using 80 fs laser pulses at 515, 800, and 1030 nm. Listed are the two-, three-, and four-absorption coefficients (β,γ,δ) along with the corresponding n-photon absorption cross sections (σ_2,σ_3, and σ_4), and the nonlinear refractive indices (n_2). Values are reported as effective nonlinear coefficients extracted from Z-scan measurements, which account for the specific focusing conditions, finite film thickness, and the resulting nonuniform axial intensity distribution. Blank entries indicate cases where another nonlinear absorption mechanism dominates the energy deposition. All values are reported in SI units.

λ	Compound	$N_0(\times 10^{22})$	z_R	$\beta(\times 10^{-13})$	$\gamma(\times 10^{-25})$	$\delta(\times 10^{-37})$	$n_2(\times 10^{-17})$	σ_2	$\sigma_3(\times 10^{-82})$	$\sigma_4(\times 10^{-114})$
(nm)		molecules/m^3	(mm)	cm/W	cm^3/W^2	cm^5/W^3	cm^2/W	GM	cm^6/s^2	cm^8/s^3
515	SZ2080^{TM}	270.6	9.8	4.5 ± 0.5	—	—	25.2 ± 4.0	6.4 ± 0.7	—	—
	IRG369	164.7		13.6 ± 2.0	—	—	4.0 ± 0.5	31.8 ± 4.0	—	—
	SZ2080^{TM}+IRG369	271.79		26.5 ± 3	—	—	32.8 ± 5.0	37.8 ± 4.0	—	—
	BIS	185.4		31 ± 5	—	—	7 ± 1	65.1 ± 10.0	—	—
	SZ2080^{TM}+BIS	271.94		58 ± 7	—	—	41 ± 6	82.6 ± 8.0	—	—
515	SZ2080^{TM}	270.6	1.0	3.0 ± 0.3	—	—	9.1 ± 1.0	4.3 ± 0.4	—	—
	IRG369	164.7		5.7 ± 0.5	—	—	2.0 ± 0.4	13.2 ± 1.0	—	—
	SZ2080^{TM}+IRG369	271.79		11.5 ± 2.0	—	—	15.5 ± 2.0	16.4 ± 3	—	—
	BIS	185.4		11.6 ± 2.0	—	—	2.9 ± 0.2	24.3 ± 4.0	—	—
	SZ2080^{TM}+BIS	271.94		19.8 ± 3.0	—	—	20.2 ± 3.0	28.2 ± 4.0	—	—
800	SZ2080^{TM}	270.6	1.6	—	67.2 ± 7.0	—	2.8 ± 0.2	—	15.9 ± 2.0	—
	IRG369	164.7		—	18.2 ± 2.0	—	3.6 ± 0.5	—	7.1 ± 0.8	—
	SZ2080^{TM}+IRG369	271.79		—	86.6 ± 10.0	—	6.7 ± 0.5	—	20.5 ± 2.0	—
	BIS	185.4		13.5 ± 2.0	—	—	5.0 ± 0.5	18.1 ± 3.0	—	—
	SZ2080^{TM}+BIS	271.94		36.2 ± 5.0	—	—	11.3 ± 2.0	33.3 ± 5.0	—	—
800	SZ2080^{TM}	270.6	0.17	—	15.7 ± 2.0	—	1.8 ± 0.2	—	3.7 ± 0.5	—
	IRG369	164.7		—	4.6 ± 0.5	—	1.3 ± 0.3	—	1.8 ± 0.2	—
	SZ2080^{TM}+IRG369	271.79		—	21.3 ± 3.0	—	3.8 ± 0.2	—	5.1 ± 0.9	—
	BIS	185.4		4.0 ± 0.2	—	—	2.2 ± 0.4	5.4 ± 0.3	—	—
	SZ2080^{TM}+BIS	271.94		13.7 ± 1.0	—	—	5.9 ± 0.8	9.4 ± 1.0	—	—
1030	SZ2080^{TM}	270.6	2.7	—	—	108 ± 12	4.1 ± 0.3	—	—	27.2 ± 3.0
	IRG369	164.7		—	1.1 ± 0.2	—	0.9 ± 0.2	—	0.43 ± 0.08	—
	SZ2080^{TM}+IRG369	271.79		—	12.6 ± 1.0	—	6.3 ± 0.8	—	3.0 ± 0.2	—
	BIS	185.4		—	2.2 ± 0.4	—	1.2 ± 0.1	—	0.8 ± 0.1	—
	SZ2080^{TM}+BIS	271.94		13.5 ± 2.0	—	—	10.0 ± 1.0	12.4 ± 2.0	—	—
1030	SZ2080^{TM}	270.6	0.25	—	—	24.3 ± 4.0	1.6 ± 0.2	—	—	6.1 ± 1.0
	IRG369	164.7		—	0.28 ± 0.03	—	0.53 ± 0.08	—	0.11 ± 0.01	—
	SZ2080^{TM}+IRG369	271.79		—	2.6 ± 0.2	—	3.5 ± 0.3	—	0.64 ± 0.04	—
	BIS	185.4		—	0.55 ± 0.06	—	0.63 ± 0.06	—	0.19 ± 0.2	—
	SZ2080^{TM}+BIS	271.94		3.1 ± 0.4	—	—	4.0 ± 0.5	2.2 ± 0.3	—	—

excitation, in contrast to the IRG369-containing sample, which exhibits 3 PA process. In addition, charge transfer induced states generally have larger transition dipole moments and a wider spatial redistribution of electrons [43], which is critical for enhanced optical nonlinearities. Consequently, the SZ2080^{TM}-BIS formulation presents more efficient electronic transitions and significantly stronger nonlinear absorptive response compared to the SZ2080^{TM}-IRG369 formulation, which lacks similar charge transfer effects. Similar charge transfer-induced enhancements in nonlinear absorption have been reported for various push-pull molecular systems (see for example refs. [19, 44–47])

As shown in Figure 3A,B, direct excitation of the states at 515 nm results in their fast saturation, observed as a transition from saturable absorption (SA) with transmission > 1 to 2 PA (transmission < 1) when the intensity exceeds approximately 120 and 300 GW/cm^2 for the 20 and 2.5 cm focal length lenses, respectively, allowing for high resolution structuring even in the presence of low linear absorption at the writing wavelength. Below this threshold, single-photon (1 PA) allowed transitions effectively populate these states, giving rise to SA. The SA-type OA Z-scan recordings, fitted with Equation (1), yielded negative nonlinear absorption coefficients of $\beta = (-32 \pm 3) \times 10^{-1}$ cm/TW (20 cm focal length) and $\beta = (-20 \pm 2) \times 10^{-1}$ cm/TW (2.5 cm focal length). At higher intensities, the SA response saturates and a dip appears at the center of the transmission maximum, indicative of a regime where the 1 and 2 PA processes coexist. In this regime, the lower energy states become fully occupied and can no longer accept more electrons, thereby further excitation begins to occur into higher energy states through two-photon absorption. Under these conditions, using the modified intensity-dependent absorption coefficient α of Equation (9), the sample's transmittance can be described by Equation (10) [48]

$$\alpha = \frac{\alpha_0}{1 + I/I_s} + \beta I \tag{9}$$

$$T(z) = \sum_{m=0}^{\infty} \frac{\left(\frac{-\alpha I_0 L_{\text{eff}}}{1+(z/z_0)^2}\right)^m}{m+1} \tag{10}$$

where α_0 is the linear absorption coefficient, β the two-photon absorption coefficient, I_s the saturation intensity, L_{eff} the sample's effective length, z_0 the Rayleigh length of the beam, and m the index of the infinite series. As shown in Figure 3C, fitting the data presenting a transition from SA to RSA with Equation (10), the values of 2 PA coefficient β in this regime were found to increase with the laser peak intensity, reaching a plateau for higher intensities where 2 PA dominates the nonlinear response. From the same equation, the saturation intensity I_s values were determined to be (0.12 ± 0.03) TW/cm^2 and (0.30 ± 0.04) TW/cm^2 for beams with Rayleigh lengths of 9.8 and 1.0 mm, respectively.

Moreover, from Figures 2 and 3, and Table 1, it is evident that the Rayleigh length of the beam critically affects the laser energy deposition, as increasing the Rayleigh length by an almost order of magnitude enhances the effective n-photon absorption coefficients and cross sections by roughly 2–4 times. In general, a larger Rayleigh length increases the spatial region over which the laser intensity is high, consequently extending the effective interaction volume. Since the n-photon absorption A scales nonlinearly with intensity as

$$A \propto I_0^n z_R C_n \tag{11}$$

where C_n is a constant that depends only on the order of the process n (see the mathematical proof in Supplementary Information Section), an increase in z_R at fixed peak intensity enhances the nonlinear interaction and correspondingly increases A. In the present case, reaching the same transmittance variations with a tenfold shorter Rayleigh length requires about twice the intensity, which accounts for the 2–4 fold enhancement of nonlinear absorption when the Rayleigh length is increased by an order of magnitude. Therefore, while the third-order susceptibility $\chi^{(3)}$ is an intrinsic material property, the experimentally determined coefficients depend on the spatial intensity distribution within the total sample thickness (≈0.15 mm) under tightly focused femtosecond excitation. It means that the nonlinear absorption and refraction coefficients are extracted as effective macroscopic parameters from Z-scan measurements. Particularly, in the case of tighter focusing, the Rayleigh range becomes comparable to the sample thickness (film and glass substrate), leading to a strong axial intensity gradient and a reduced volume-integrated nonlinear response, as only a fraction of the sample experiences peak intensity. Conversely, for looser focusing (larger beam waist), the intensity remains nearly

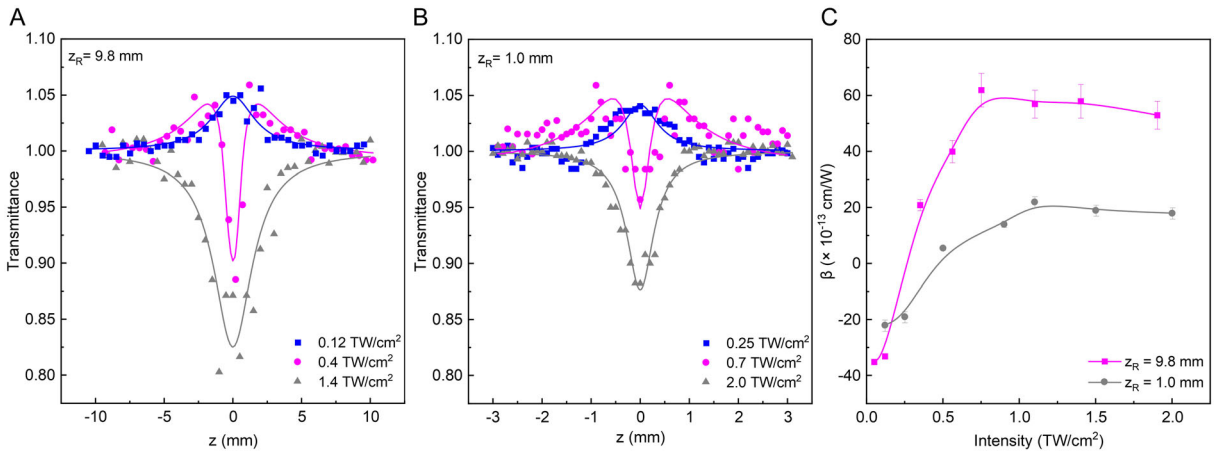

FIGURE 3 | (A), (B) Intensity-dependent OA Z-scans of SZ2080^{TM} mixed with BIS at 515 nm under different focusing configurations, presenting a transition from saturable absorption to two-photon absorption with increasing the incident laser intensity. (C) Variation of the corresponding two-photon absorption coefficients β as a function of the laser peak intensity.

uniform across the entire thickness, enabling a larger effective interaction volume and a stronger cumulative nonlinear signal. In this case, the extracted coefficients match the intrinsic material property. Consequently, the Z-scan fitting procedure captures this geometry-dependent, volume-averaged response as variations in the effective values, without implying any change in the intrinsic third-order nonlinearity of the material. A detailed definition of the effective coefficients is provided in the Supplementary Information Section, along with a mathematics approximation that correlates the measured effective coefficients to the intrinsic material properties in the tight focusing regime used in laser-based lithography. This interpretation is consistent with thin-to-intermediate sample regimes and provides a physically accurate description of nonlinear energy deposition under multiphoton 3D lithography-relevant irradiation conditions.

Moreover, due to the high peak intensities required to induce measurable nonlinear signals, photogenerated free carriers (e.g., free-carrier absorption and free-carrier–induced refractive index changes) are expected to contribute partially to the nonlinear coefficients. Under tighter focusing, the smaller interaction volume and stronger spatial intensity gradients may also enhance carrier diffusion out of the focal region, thus reducing their residence time within the interaction volume. As a result, the cumulative free-carrier absorption and refractive contributions to the volume-integrated Z-scan signal may be slightly reduced, leading to lower extracted effective coefficients.

Specifically, in the context of MPL, these findings indicate that lower-NA objectives enhance the deposited energy dose per pulse, leading to reduced laser intensities needed for initiating polymerization, which in turn lowers the operation costs and enhances the fabrication throughput. However, many advanced photonic applications (e.g., photonic crystals and waveguides) may require the highest possible spatial resolution for precise light control. In these cases, higher-NA objectives remain essential to achieve the necessary nanoscale precision. In contrast, lower-NA objectives are often used for printing large-area 3D structures, such as biomedical scaffolds, microelectromechanical systems, and microrobotic assemblies, where ultrahigh resolution is not the key requirement. In both cases, however, the knowledge of nonlinear properties provides insights into the experimental conditions that enable the most effective energy deposition.

3.3 | Nonlinear Refraction Properties

CA Z-scan measurements of pure and photosensitized SZ2080^{TM}, shown in Figure 4A–F, reveal a characteristic valley-peak configuration, corresponding to self-focusing and a positive nonlinear refractive index n_2. These measurements were conducted under similar excitation conditions used to study the MPA absorption properties of the samples. The observed behavior arises from an ultrafast electronic nonlinearity, that is, the instantaneous distortion of the electronic cloud in the strong fs laser field. Contributions from thermal lensing are negligible under our experimental conditions, as thermal effects typically lead to self-defocusing, in the long run [29, 49], which was not observed. Furthermore, no temporal evolution of the signal or dependence on the irradiated sample locations were detected, confirming the absence of heat accumulation. Both BIS and IRG369 solutions likewise displayed a self-focusing response (see Figure S2).

In all measurements, in contrast to the glass substrate, which exhibited very small nonlinear refraction signal, the solvent (i.e., DCM) contributed a significant self-focusing signal. This background was removed to extract the nonlinear refractive indices n_2 of the samples, and the resulting values within a range of laser intensities, as well as their average values, are presented in Figure 4G–I and Table 1, respectively.

These values show that, in most cases, SZ2080^{TM} possesses a stronger nonlinear refraction than both photosensitizers. Thus, in the SZ2080^{TM}/photosensitizer mixtures, the refractive nonlinear response is overwhelmingly dominated by the pre-polymer, which is expected given its almost 100-fold larger weight fraction compared to the photosensitizer. The addition of the photosensitizers led to a pronounced increase in the n_2 values of the pre-polymer under all excitation regimes, with the largest variation (2–3 times) occurring in the BIS-containing formulation, attributed to charge transfer effects discussed earlier. The observed decreasing trend of n_2 from the visible to the infrared, followed by its nearly constant values in the infrared region, can be explained by the modified Kramers–Kronig relations, which predict a 'normal adispersion-like' response of the nonlinear refractive index n_2 as long as the excitation wavelength remains detuned from absorption band resonance [50].

In addition to the compositional effects, the extend of Rayleigh length influenced the nonlinear refraction. Particularly, the decrease of the Rayleigh length by approximately one order of magnitude caused a 2-3-fold decrease in the n_2 values, consistent with the behavior observed for nonlinear absorption. This decrease arises from the shorter nonlinear propagation of the beam, which confines the phase change accumulation within a more localized focal volume.

In MPL, the knowledge of n_2 is also essential as any significant intensity-dependent variation of the refractive index n can modify beam propagation and distort the focal volume, leading to degradation of spatial resolution. However, as shown in Supplementary Section, the self-focusing induced nonlinear propagation has only a minor contribution to the intensity-dependent refractive index change in both pure and photosensitized SZ2080^{TM}, as the condition $n_2 I \ll n_0$ is fulfilled under all excitation regimes. Hence, the refractive index change is too small to introduce beam-propagation distortions or focal-volume broadening, ensuring the accurate energy confinement within the voxel volume. This provides a clear explanation of the unchanged feature sizes in 3D microstructures observed in previous reports [24, 25], regardless of whether a photosensitizer is mixed with the host prepolymer.

To further demonstrate that the contribution of self-focusing is negligible under the tight-focusing conditions used in laser-based 3D printing, the nonlinear propagation lengths L_n (i.e., the distance at which the phase differs by 2π because of nonlinear refraction) were also calculated (see Supplementary Section). From the determined L_n values, it is concluded that for the nonlinear refraction to have an effect on beam propagation, the wave would need to travel a distance larger than the Rayleigh length of the high-NA focused beams (NA > 0.7) typically used in 3D photopolymerization. Consequently, self-focusing does not affect significantly the voxel dimensions and spatial resolution.

A clear sign reversal of n_2 was also observed in the CA Z-scan (see Figure S3) only at much higher laser intensities than those used for assessing the electronic contribution to the refractive

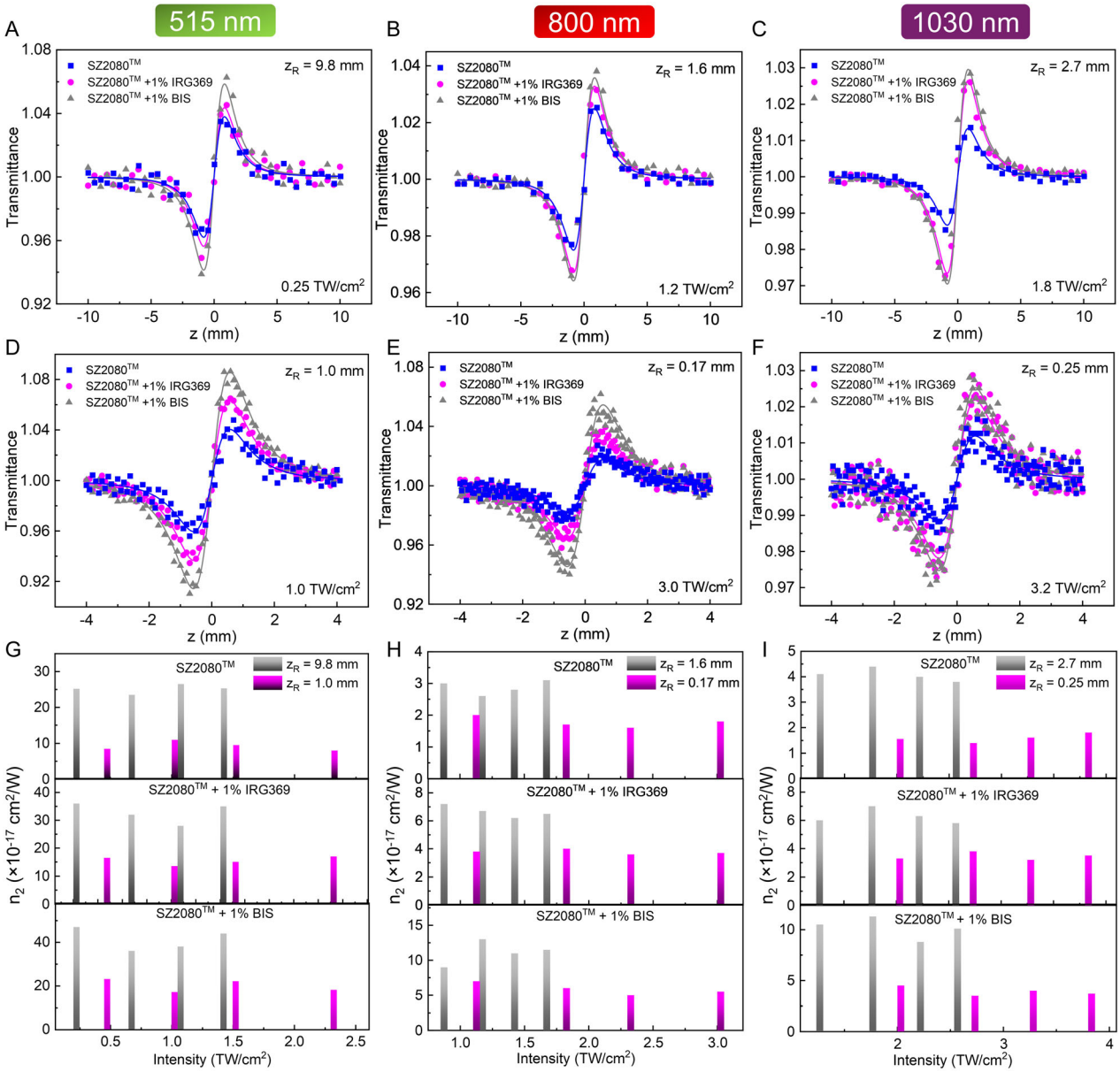

FIGURE 4 | CA Z-scan recordings and nonlinear refractive indices of SZ2080™ with and without photosensitizers under different laser peak intensities and two focusing configurations at (A), (D), (G) 515 nm, (B), (E), (H) 800 nm, and (C), (F), (I) 1030 nm. Tighter focusing required significantly higher intensities to detect nonlinear refraction signal.

index change, particularly in the samples that exhibited 2 PA at the investigated wavelengths. For instance, under 515 nm irradiation, SZ2080™ exhibited a negative $n_2 = (-31.3 \pm 4.0) \times 10^{-17}$ cm²/W at an intensity of about 1.7 TW/cm² when measured using a beam with Rayleigh length $z_R = 9.8$ mm, while a reduced value of $n_2 = (-5.3 \pm 0.7) \times 10^{-17}$ cm²/W, corresponding to an intensity of about 3.7 TW/cm², was measured with a more tightly focused beam of $z_R = 1.0$ mm. Given the absence of thermal effects under our experimental conditions, the observed sign inversion of n_2 can be therefore assigned to free-carrier generation through multiphoton and/or avalanche ionization, resulting in a defocusing contribution that increases with the carrier density. Free carrier generated through multiphoton ionization typically appear on femtosecond timescales, nearly simultaneously with the laser pulse, whereas avalanche ionization follows more gradually, building up free carriers over picoseconds through electron impact processes [51]. Such free-carrier induced nonlinearities are typically associated with a self-defocusing response, arising from the higher carrier density generated at the beam center relative to its periphery, and can be effectively characterized by employing the Z-scan technique [52, 53]. As the carriers' density increases, the free-carrier-induced defocusing can eventually obscure the Kerr self-focusing effect. A very large free-carrier population results in dielectric breakdown, which reduces the real part of permittivity ε' to zero ($\varepsilon' = n^2 - \kappa^2 \equiv 0$), and increases the imaginary part ε'' to the value $\varepsilon'' = 2n\kappa$. This leads to a complex refractive index $\tilde{n} = \sqrt{\varepsilon' + i\varepsilon''} = n + i\kappa$ dominated by its imaginary part, and thus the material becomes highly reflective and absorptive, with an absorption coefficient $\alpha = 4\pi\kappa/\lambda$. The determined n_2 values are also very useful for optimizing theoretical models of voxel shape and its evolution during 3D printing [54].

3.4 | Analysis of Polymerized 3D Structures Fabricated via MPL

The multiphoton absorption and refraction properties presented above provide a clear picture of the photopolymerization behavior of SZ2080^{TM}-based resists. More precisely, the refractive index variation, the nonlinear absorption coefficients, the order of MPA process, and the degree of axial beam confinement together determine the accuracy and efficiency of energy deposition within the focal volume. Thus, these parameters are expected to impact both the polymerization threshold and the attainable spatial resolution. To qualitative correlate the determined nonlinear properties with the polymerization performance of mixtures with and without photosensitizers, and to verify the Z-scan results showing that the axial extent of nonlinear energy deposition influences the polymerization efficiency, the bridge-structure method, presented schematically in Figure 5a, was used under tight-focusing conditions employing objectives with NA = 1.4 and NA = 0.45. In this approach, arrays of single-scan lines are fabricated while periodically increasing the radiation intensity after each line, beginning from the minimum intensity that produces a continuous and mechanically stable suspended bridge without discontinuities or collapse until the intensity at which overexposure becomes visible [24].

Representative bridge structures fabricated under two different axial beam-confinement conditions using pure SZ2080^{TM} and SZ2080^{TM} mixed with 1 wt% BIS and IRG369 are presented in Figure 5b,c as an example. Statistical analysis of the bridge structures, fabricated using different batch of samples, was used to precisely extract the values of polymerization threshold. These values, shown in Figure 5d,e, reveal a lower polymerization threshold for the photosensitized SZ2080^{TM} compared to the pure prepolymer in agreement with previous reports [24, 25]. This behavior attributed to their reduced MPA order and the enhanced nonlinear optical properties arising from the strong interaction between the prepolymer matrix and the photosensitizers, with the host matrix itself contributing decisively in the deposition of energy, as evidenced by the Z-scan results.

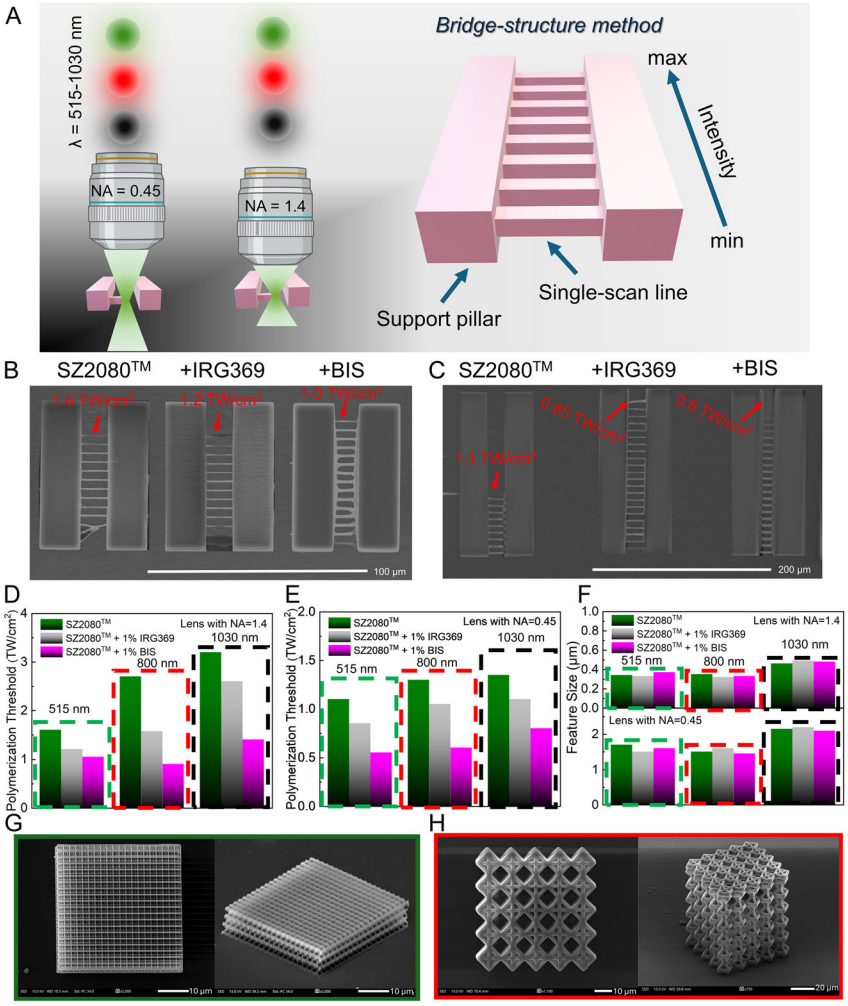

FIGURE 5 | (A) Schematic of the bridge-structure method employed to assess the polymerization thresholds and lateral voxel dimension under two different axial confinement regimes, using objective lenses with NA = 0.45 and NA = 1.4 at excitation wavelengths of 515–1030 nm. (B, C) Representative SEM images of bridge structures fabricated using (B) a high-NA objective (NA = 1.4) and (C) a lower-NA objective (NA = 0.45), showing the polymerization thresholds of pure and photosensitized SZ2080^{TM} under 515 nm laser irradiation. (D, E) Extracted polymerization thresholds at 515, 800, and 1030 nm using (D) NA = 1.4 and (E) NA = 0.45 objective lenses. (F) Corresponding feature dimensions under both focusing conditions. (G, H) Examples of complex 3D microarchitectures fabricated through MPL: (G) a woodpile photonic crystal printed in neat SZ2080^{TM} under 515 nm excitation, and (H) a complex 3D scaffolds printed in BIS-formulated SZ2080^{TM} resist under 800 nm excitation.

Among the two photosensitized prepolymers studied in this work, the BIS-containing formulation exhibited lower polymerization thresholds than the corresponding IRG369-containing formulation under all excitation wavelengths. This is probably attributed to the formation of an efficient complex donor–acceptor system given the strong electron-donating character of the dimethylamino groups of BIS. The resulting charge transfer states in the visible spectral region enhances the nonlinear response and decreases the MPA order, which lead to an improved rate of polymerization through more deposition of energy within the focal volume.

Furthermore, the analysis of the bridge structures showed that the axial confinement of the focused beam can be controlled to achieve more efficient deposition of energy. Particularly, the lines fabricated with an objective lens of NA = 0.45 exhibited lower polymerization thresholds (approximately half) compared to those fabricated using an objective of NA = 1.4, due to increased interaction volume. This trend follows that of the measured nonlinear coefficients, which present enhancement with increasing the Rayleigh range. Additionally, this trend is consistent with the OA Z-scan findings, showing that approximately the double laser intensity is required to induce the same transmittance variation when the effective interaction volume is reduced tenfold. It should be noting that a direct correlation between the nonlinear coefficients and variations in polymerization thresholds with increasing the interaction volume is valid, as for both Z-scan and MPL experiments, the beams used had Rayleigh lengths differing by 10 times. Thus, supported by the determined nonlinear coefficients, it is nicely demonstrated that the spatial extension of laser beam confinement can lead to more energy-efficient 3D fabrication, thereby decreasing energy consumption and mitigating unwanted photodamage.

The bridge structure method was further used for assessing the achievable spatial resolution in pure and photosensitized SZ2080^{TM}. In this procedure, the minimum possible line width, printed without any indication of overexposure or structural collapse, was measured. The extracted feature sizes are presented in Figure 5f, where it can be seen that the lateral dimension of the lines remains practically unchanged under all excitation wavelengths and focusing regimes, regardless of the presence of a photosensitizer in the mixture. The resulting feature sizes therefore, reflect the minimal influence of the photosensitizers on the voxel dimensions, consistent with the very small refractive index changes introduced by their addition, which ensures energy deposition confined with high precision as discussed above. Moreover, different orders of nonlinear absorption did not translate into significant differences in the lateral feature size measured close to the polymerization threshold in agreement with previous observations [24]. It is noteworthy that the BIS-containing resist shows increased features sizes and reduced structure fidelity at 515 nm, attributed to thermal effects facilitated by the high repetition rate and the low linear absorption at the excitation wavelength. The feature sizes reported here reflect the selected processing conditions rather than the ultimate resolution limit of the materials.

Most importantly, the present work provide the first experimental evidence that the pure resist can initiate effectively polymerization through two-, three-, and four-photon absorption processes because of its dominant contribution to the nonlinear energy deposition. As a result, the pure resist itself enables the precise fabrication of complex 3D architectures, such as those presented in Figure 5g,h. This finding is of high importance for the broader community of AM, as it establishes a 'greener' manufacturing approach through the elimination of toxic photosensitizers. This approach also eliminates several other disadvantages associated with the use of photosensitizers, such as their cytotoxicity that limits bio-related applications [55], the unwanted coloration of the final structure, and the strong auto-fluoresence that generates background signals and compromises fluorescence-based imaging or sensing [56].

A primary challenge in comparing MPL performance across different wavelengths is the variation in laser architectures, particularly in pulse duration and repetition rate. In the present work, the use of different fiber-based laser systems relevant to 3D printing induces confounding variables that prevent a perfectly isolated comparison of nonlinear properties in different excitation regimes. The agreement between the measured nonlinear coefficients and the observed printing trends supports the interpretation that nonlinear energy deposition remains the dominant mechanism, while acknowledging that cumulative thermal effects become increasingly relevant at high repetition rates. An ideal experiment would maintain identical spectrotemporal excitation conditions for the Z-scan measurements and MPL demonstrations. Future studies using tunable, dispersion-compensated OPA systems operated at similar repetition rate ranges will be necessary to entirely decouple electronic nonlinearities from cumulative thermal effects.

By determining the nonlinear coefficients of pure and photosensitized SZ2080^{TM} resists and quantifying how the nonlinear absorption and refraction vary with the Rayleigh length, we establish a framework for the precise modeling of energy deposition within the voxel volume, allowing for precise energy control in 3D micro- and nanoprinting. This approach provides a reliable prediction of the onset of polymerization and the achievable spatial resolution under all the commercially available laser wavelengths and focusing conditions without extensive parametric trials, thus substantially accelerating the optimization of fs-laserbased 3D printing.

4 | Conclusions

The underlying physical processes of fs-laser-based polymerization were elucidated for first time by investigating how interactions between the host prepolymer and the photosensitizers influence the energy deposited within the focal volume. This investigation was performed by determining the multiphoton absorption and nonlinear refraction coefficients of the SZ2080^{TM} resist, the photosensitizers BIS and IRG369, and their corresponding formulations through the Z-scan technique under all the excitation wavelength relevant to MPL.

The results revealed that the photosensitizers interact strongly with the SZ2080^{TM} prepolymer, resulting in a decrease of the effective order of MPA and a concomitant enhancement of the energy deposited within the focal volume. The deposited energy dose per pulse was found to arise from cumulative contributions from both the photosensitizers and the host prepolymer. However, because of its almost 100 times larger weight fraction, the prepolymer contributes significantly to the nonlinear optical response under all excitation regimes. As a result, the pure resist can effectively initiate polymerization itself through two-, three-, or even four-photon absorption without the use of potentially toxic photosensitizers,

promoting a 'greener' 3D AM approach. This finding represents a breakthrough for the MPL, as it challenges the traditional assumption that photo-polymerization is initiated exclusively by the photosensitizers and/or photoinitiators.

Notably, it was show that more efficient nonlinear excitation can be achieved by extending the beam Rayleigh length, which mitigates photodamage, thus enhancing the throughput in MPL when using lower NA objectives.

The determined nonlinear absorption and refraction properties of pure and photosensitized SZ2080^{TM}, and the quantification of their dependence on the axial extent of the interaction volume, under all excitation wavelengths relevant to MPL, enable the precise control of nonlinear energy delivery during 3D printing. This approach accounts for the previously overlooked contribution of the prepolymer matrix itself to the deposited energy. As a result, this study allows for the prediction/estimation of laser energies required to initiate polymerization and of the attainable spatial resolution for different focusing configurations, thus avoiding extensive empirical parameter trials. This study has established a physics-based foundation for rational optimization and scaling of the 3D printing process.

Acknowledgments

M.S, M.F, and D.G gratefully acknowledge NAIAD cofunded by the Stavros Niarchos Foundation (SNF) and the Hellenic Foundation for Research and Innovation (H.F.R.I.) under the fifth Call of "Science and Society" Action–"Always Strive for Excellence–Theodore Papazoglou" (project no. 9578.), as well as the European Union's Horizon Europe research and innovation program under grant agreement no. 101091644. U.K. participants in Horizon Europe Project FABulous are supported by UKRI grant no. 10062385 (MODUS). M.S, G.Z, D.L, and M.M carried out research in the framework of the "Universities Excellence Initiative" programme by the Ministry of Education, Science and Sports of the Republic of Lithuania under the agreement with the Research Council of Lithuania (project no. S-A-UEI-23–6). S.J. was supported via ARC DP240103231 grant and is grateful for the research stay at the Laser Research Center (VU), Vilnius in 2025. G.Z. acknowledges support from Vilnius University under the Vilnius University Postdoctoral Fellowships Scheme. G.Z. and D.L. also acknowledge support from the Vilnius University Foundation under the 2024 Co-Funding Competition award. M.S acknowledges support from LaserlabEurope (Laserlab4 EU) under PID 36533 – VULRC (JE). All the authors thank Aleka Manousaki for her support in recording the SEM images.

The publication of this article in OA mode was financially supported by HEAL-Link.

Funding

This study was supported by Stavros Niarchos Foundation (9578), Hellenic Foundation for Research and Innovation (9578), European Union's Horizon Europe (101091644, 0062385), Universities Excellence Initiative (S-A-UEI-23–6), ARC DP240103231, Laserlab-Europe (PID 36533 – VULRC (JE)), Vilnius University. The publication of the article in OA mode was financially supported by HEAL-Link.

Conflicts of Interest

The authors declare no conflicts of interest.

References

1. M. Farsari and B. N. Chichkov, "Two-Photon Fabrication," *Nature Photonics* 3 (2009): 450–452.

2. M. Malinauskas, A. Zukauskas, S. Hasegawa, et al., "Ultrafast Laser Processing of Materials: From Science to Industry," *Light: Science and Applications* 5 (2016): e16133.

3. H. Wang, W. Zhang, D. Ladika, et al., "Two-Photon Polymerization Lithography for Optics and Photonics: Fundamentals, Materials, Technologies, and Applications," *Advanced Functional Materials* 33, no. 39 (2023): 2214211.

4. N. Shahrubudin, T. Lee, and R. Ramlan, "Procedia Manufacturing," in 2nd International Conference on Sustainable Materials Processing and Manufacturing (SMPM, 2019) pp. 8–10.

5. G. Zyla and M. Farsari, "Frontiers of Laser-Based 3D Printing: A Perspective on Multi-Photon Lithography," *Laser and Photonics Reviews* 18, no. 7 (2024): 2301312.

6. V. Harinarayana and Y. Shin, "Two-Photon Lithography for Three-Dimensional Fabrication in Micro/Nanoscale Regime: A Comprehensive Review," *Optics Laser Technology* 142 (2021): 107180.

7. E. Skliutas, G. Merkininkaite, S. Maruo, et al., "Multiphoton 3D Lithography," *Nature Reviews Methods Primers* 5 (2025): 15.

8. F. Chen, S. Shi, S. Xue, et al., "Recent Advances and Challenges in Multi-Photon 3D Nanoprinting," *Engineering* 49 (2025): 13.

9. W. Wang, Z.-Q. Chen, B. Lin, et al., "Two-Photon Polymerization-Based 3D Micro-Scaffolds toward Biomedical Devices," *Chemical Engineering Journal* 493 (2024): 152469.

10. D. Gonzalez-Hernandez, S. Varapnickas, A. Bertoncini, C. Liberale, and M. Malinauskas, "Micro-Optics 3D Printed via Multi-Photon Laser Lithography," *Advanced Optical Materials* 11, no. 1 (2023): 2201701.

11. G. Zyla, G. Maconi, A. Nolvi, et al., "3D Micro-Devices for Enhancing the Lateral Resolution in Optical Microscopy," *Light: Advanced Manufacturing* 5 (2024): 19.

12. S. Papamakarios, O. Tsilipakos, I. Katsantonis, et al., "Cactus-Like Metamaterial Structures for Electromagnetically Induced Transparency at THz Frequencies," *ACS Photonics* 12, no. 1 (2025): 87.

13. G. Zyla, S. Papamakarios, D. C. Zografopoulos, et al., "Film-Based Multi-Photon Lithography for Efficient Printing of Electromagnetic Surface Structures," *Advanced Materials Technologies* 10, no. 11 (2025): 2402137.

14. R. Ziolkowski, "Design, Fabrication, and Testing of Double Negative Metamaterials," *IEEE Transactions on Antennas and Propagation*, 51, no. 7 (2003): 1516.

15. V. Matining, C. Colli, E. Mauri, and D. Moscatelli, "Advances in Microfluidics: From State-of-the-Art to Two-Photon Polymerization 3D Printing Perspectives," *Applied Materials Today* 47 (2025): 102953.

16. R. L. Sutherland, *Handbook of Nonlinear Optics* (Marcel Dekker, 1998).

17. R. W. Boyd, *Nonlinear Optics*, (Academic Press, 2003).

18. P. Somers, A. M. ñichinger, S. Maruo, C. Moser, X. Xu, and M. Wegener, "The Physics of 3D Printing with Light," *Nature Reviews Physics* 6 (2024): 99.

19. M. Stavrou, G. Zyla, D. Ladika, F. Dumur, M. Farsari, and D. Gray, "Push–Pull Carbazole-Based Dyes: Synthesis, Strong Ultrafast Nonlinear Optical Response, and Effective Photoinitiation for Multiphoton Lithography," *ACS Applied Optical Materials* 2, no. 8 (2024): 1653.

20. D. Ladika, M. Stavrou, G. Zyla, et al., "High- and Low-Fluorescent Photoinitiators for Multiphoton Lithography," *ACS Applied Polymer Materials* 7 (2025): 15–10120.

21. L. V. Keldysh, "Ionization in the Field of a Strong Electromagnetic Wave," *JETP* 20, no. 5 (1964): 1945.

22. F. Jin, J. Liu, Y.-Y. Zhao, X.-Z. Dong, M.-L. Zheng, and X.-M. Duan, *Nature Communications* 13, no. 1 (2022): 1357.

23. Y. Bougdid and Z. Sekkat, "Voxels Optimization in 3D Laser Nanoprinting," *Scientific Reports* 10, no. 1 (2020): 10409.

24. E. Skliutas, D. Samsonas, A. Ciburys, et al., "X-Photon Laser Direct Write 3D Nanolithography," *Virtual and Physical Prototyping* 18, no. 1 (2023): e2228324.

25. D. Ladika, A. Butkus, V. Melissinaki, et al., "X-Photon 3D Lithography by FS-Oscillators: Wavelength-Independent and Photoinitiator-Free," *Light: Advanced Manufacturing* 5, no. 4 (2024): 567.

26. M. Stavrou, D. Ladika, E. Skliutas, et al., "Direct Measurement of Two-photon Absorption and Refraction Properties of SZ2080^{TM} -based Resists at 515 nm: Insights into 3D Printing," *Nanophotonics* 14, no. 18 (2025): 2981.

27. B. Gu, C. Zhao, A. Baev, K.-T. Yong, S. Wen, and P. N. Prasad, "Molecular Nonlinear Optics: Recent Advances and Applications," *Advances in Optics and Photonics* 8, no. 2 (2016): 328.

28. D. N. Christodoulides, I. C. Khoo, G. J. Salamo, G. I. Stegeman, and E. W. V. Stryland, "Nonlinear Refraction and Absorption: Mechanisms and Magnitudes," *Advances in Optics and Photonics* 2, no. 1 (2010): 60.

29. M. Stavrou, I. Dalamaras, N. Karampitsos, and S. Couris, "Determination of the Nonlinear Optical Properties of Single- and Few-Layered Graphene Dispersions under Femtosecond Laser Excitation: Electronic and Thermal Origin Contributions," *The Journal of Physical Chemistry C* 124, no. 49 (2020): 27249.

30. P. Gao, E. da Silva, L. Hou, N. D. Denslow, P. Xiang, and L. Q. Ma, "Human Exposure to Polycyclic Aromatic Hydrocarbons: Metabolomics Perspective," *Environment International* 119 (2018):466.

31. M. Malinauskas, A. Zukauskas, G. Bi˘ckauska, and R. Gadonas, "Mechanisms of Three-Dimensional Structuring of Photo-Polymers by Tightly Focussed Femtosecond Laser Pulses," *Optics Express* 18, no. 10 (2010): 10209.

32. D. Samsonas, E. Skliutas, A. Ciburys, et al., "3D Nanopolymerization and Damage Threshold Dependence on Laser Wavelength and Pulse Duration," *Nanophotonics* 12, no. 8 (2023): 1537.

33. J. B. Mueller, J. Fischer, F. Mayer, M. Kadic, and M. Wegener, "Polymerization Kinetics in Three-Dimensional Direct Laser Writing," *Advanced Materials* 26, no. 38 (2014): 6566.

34. M. Sheik-Bahae, A. A. Said, and E. W. V. Stryland, "High-Sensitivity, Single-Beam n_2 Measurements," *Optics Letters* 14 (1989): 17–955.

35. D. S. Corr^ea, L. D. Boni, L. Misoguti, I. Cohanoschi, F. E. Hernandez, and C. R. Mendon¸ca, "Z-Scan Theoretical Analysis for Three-, Four- and Five-Photon Absorption," *Optics Communications* 277, no. 2 (2007): 440.

36. M. Sheik-Bahae, A. Said, T.-H. Wei, D. Hagan, and E. Van Stryland, "Sensitive Measurement of Optical Nonlinearities Using a Single Beam," *IEEE Journal of Quantum Electronics* 26, no. 4 (1990): 760.

37. A. Ovsianikov, J. Viertl, B. Chichkov, et al., "Ultra-Low Shrinkage Hybrid Photosensitive Material for Two-Photon Polymerization Microfabrication," *ACS Nano* 2, no. 11 (2008): 2257.

38. E. J. J. Groenen and W. N. Koelman, "Spectroscopic Study of Michler's Ketone. Part 1.—Absorption," *Journal of the Chemical Society, Faraday Transactions 2* 75 (1979): 58.

39. V. H. Rezvan, "Charge Transfer Complexes: A Review Survey," *Results in Chemistry* 17 (2025): 102600.

40. , T. Rijavec, S. Bra˘cko, and I. L. Van Langenhove, *Smart Textiles for Medicine and Healthcare*, (Woodhead Publishing, 2007) pp. 978.

41. N. V. Kamanina, V. S. Vikhnin, A. Leyderman, A. Barrientos, Y. Cui, and M. Vlasse, "Effect of Fullerenes C60and C70 on the Absorption Spectrum of 2-Cyclooctylamino-5-Nitropyridine," *Optics and Spectroscopy* 89, no. 3 (2000): 369.

42. M. Liu, M.-D. Li, J. Xue, and D. L. Phillips, "Determination of the Rate Constant for the $OH(X^2\pi) + OH(X^2\pi) \rightarrow H_2O + O(^3P)$ Reaction Over the Temperature Range 295 to 701 K," *The Journal of Physical Chemistry A* 118 (2014): 38–8701.

43. J.-L. Br'edas, D. Beljonne, V. Coropceanu, and J. Cornil, "Impact of Packing Arrangement on the Optical Properties of C60 Cluster Aggregates," *Chemical Reviews* 104 (2004): 11–4971.

44. S. Semin, X. Li, Y. Duan, and T. Rasing, "Nonlinear Optical Properties and Applications of Fluorenone Molecular Materials," *Advanced Optical Materials* 9 (2021): 23–2100327.

45. M. Khalid, H. M. Lodhi, M. U. Khan, and M. Imran, "Structural Parameter-Modulated Nonlinear Optical Amplitude of Acceptor–π–D–π–donor-Configured Pyrene Derivatives: A DFT Approach," *RSC Advances* 11 (2021): 14237.

46. D.-J. Li, Q.-h. Li, Z.-R. Wang, Z.-Z. Ma, Z.-G. Gu, and J. Zhang, "Intramolecular London Dispersion Interactions Do Not Cancel in Solution," *Journal of the American Chemical Society* 143 (2021): 41–17162.

47. M. Stavrou, B. Chacon, M. Farsari, et al., "Emerging Ta_4C_3 and $Mo_2Ti_2C_3$ MXene Nanosheets for Ultrafast Photonics," *Advanced Optical Materials* 13 (2025): 15–2403277.

48. M. Stavrou, N. Chazapis, E. Nikoli, R. Arenal, N. Tagmatarchis, and S. Couris, "Crystalline Phase Effects on the Nonlinear Optical Response of MoS_2 and WS_2 Nanosheets: Implications for Photonic and Optoelectronic Applications," *ACS Applied Nano Materials* 5 (2022): 11–16686.

49. M. Falconieri, "Thermo-Optical Effects in Z -Scan Measurements Using High-Repetition-Rate Lasers," *Journal of Optics A: Pure and Applied Optics* 1, no. 6 (1999): 662.

50. C. B. 'ee, A. Demircan, and G. Steinmeyer, "Kramers-Kronig Relations and High-Order Nonlinear Susceptibilities," *Physical Review A* 85 (2012): 033806.

51. B. Rethfeld, D. S. Ivanov, M. E. Garcia, and S. I. Anisimov, "Modelling Ultrafast Laser Ablation," *Journal of Physics D: Applied Physics* 50 (2017): 19–193001.

52. A. A. Said, M. Sheik-Bahae, D. J. Hagan, et al., "Determination of Bound-Electronic and Free-Carrier Nonlinearities in ZnSe, GaAs, CdTe, and ZnTe," *Journal of the Optical Society of America B* 9, no. 3 (1992): 405.

53. K. Bindra, C. Singh, and S. Oak, "Direct Measurement of Free Carrier Nonlinearity in Semiconductor-Doped Glass with Picosecond Pump–probe Z-Scan Experiment," *Optics Communications* 271, no. 1 (2007): 248.

54. V. Sedova, F. Ogor, J. Rovera, et al., "Advances in Modeling and Optimization for Two-Photon Lithography," *Journal of Micro/Nanopatterning, Materials, and Metrology* 24, no. 02 (2025): 023001.

55. M. G. Bredell, E. Besic, C. Maake, and H. Walt, "The Application and Challenges of Clinical PD–PDT in the Head and Neck Region: A Short Review," *Journal of Photochemistry and Photobiology B: Biology* 101, no. 3 (2010): 185.

56. W. Hwang, T. McPartland, S. Jeong, and C. L. Evans, "A Robust Method for Autofluorescence-Free Immunofluorescence Using High-Speed Fluorescence Lifetime imaging microscopy," *Scientific Reports* 15, no. 1 (2025): 5503.

Supporting Information

Additional supporting information can be found online in the Supporting Information section.